Defect states and room temperature ferromagnetism in cerium oxide nanopowders prepared by decomposition of Ce-propionate

Mihalache, V. ; Grivel, J. C.; Secu, M.

Published in:
Materials Chemistry and Physics

Link to article, DOI:
10.1016/j.matchemphys.2018.01.053

Publication date:
2018

Document Version
Peer reviewed version

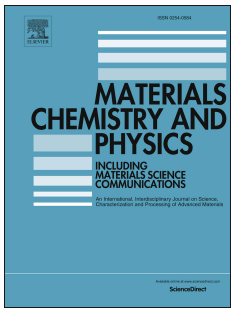

Defect states and room temperature ferromagnetism in cerium oxide nanopowders prepared by decomposition of Ce-propionate

V. Mihalache, M. Secu, J.C. Grivel

PII: S0254-0584(18)30053-1

DOI: 10.1016/j.matchemphys.2018.01.053

Reference: MAC 20325

To appear in: *Materials Chemistry and Physics*

Please cite this article as: V. Mihalache, M. Secu, J.C. Grivel, Defect states and room temperature ferromagnetism in cerium oxide nanopowders prepared by decomposition of Ce-propionate, *Materials Chemistry and Physics* (2018), doi: 10.1016/j.matchemphys.2018.01.053

- Cerium oxide nanopowders were produced by decomposition of Ce-propionate
- All samples show RTFM and a broad defect-related photoluminescence emission
- Sources for defects/oxygen vacancies potential to induce RTFM were identified
- RTFM was improved by annealing the nanoceria containing Ce2O2CO3 traces
- Decomposition of $Ce_2O_2CO_3$ at the GBs/surfaces gives an excess of oxygen vacancies

Defect states and room temperature ferromagnetism in cerium oxide nanopowders prepared by decomposition of Ce-propionate

V. Mihalache[*1], M. Secu[1], J. -C. Grivel[2]

1 National Institute of Materials Physics, P.O. Box MG-7, Bucharest-Magurele, 077125, Romania
2 Technical University of Denmark, Frederiksborgvej 399, DK – 4000 Roskilde, Denmark

***Corresponding author**: Valentina Mihalache

Tel: +40213690170

Fax: +40213690177

E-mail address: valentina.mihalache@infim.ro

Abstract

Four batches of cerium oxide powders (with nanocrystallite size of 6.9 nm - 572 nm) were prepared from four precursor nanopowders by thermal decomposition of Ce-propionate and annealing in air between 250°C – 1200°C for 10 min – 240 min. Ceria formation reactions, structure, vibrational, luminiscence and magnetic properties were investigated by differential scanning calorimetry, x-ray diffraction, electron microscopy, infrared spectroscopy, photoluminescence and SQUID. All the samples exhibit room temperature ferromagnetism, RTFM, (with coercivity, H_c, of 8 Oe - 121 Oe and saturation magnetization, M_s, of up to $6.7*10^{-3}$ emu/g) and a broad defect-related photoluminescence, PL, emission in the visible range. The samples derived from the same precursor show M_s proportional to the peak area of defect-related PL emission whereas this is not valid for the samples derived from the different precursors. An improvement of ferromagnetism and intensity of defect-related PL emission was observed when annealing the products in which nanocrystalline cerium oxide coexists with Ce - oxicarbonate traces, $Ce_2O_2CO_3$. The experimental results were explained based on the following considerations: room temperature ferromagnetism was induced by the defective ceria with high concentration of oxygen vacancies generated by decomposition of Ce-propionate; oxygen

vacancies of the starting precursor nanopowders could be redistributed (at the surfaces/grain boundaries, GBs) upon heating under conditions that promote an inert local environment; the decomposition of $Ce_2O_2CO_3$ residues can provide an excess of oxygen vacancies at the nanoparticles surfaces or GBs, which can induce or enhance ferromagnetism; surfaces/GBs rather than bulk defects appear responsible for RTFM – this can explain the (often reported in literature) inconsistency between oxygen vacancies concentration and M_S.

Keywords: Cerium oxide nanopowders; Ce – propionate; $Ce_2O_2CO_3$; ferromagnetism; photoluminescence

1 Introduction

Room temperature ferromagnetism (RTFM) shown by un-doped and transition metal (TM) doped CeO_2 [1- 3] (an otherwise nonmagnetic insulating oxide [4]), good transparency to the visible light and because its face centered cubic fluorite crystal structure matches intimately to silicon, makes ceria a potential candidate for use in future (semiconductor) spintronics, magnetooptic, magnetoelectronic and other advanced multifunctional devices [5, 6]. The ferromagnetism in cerium oxide, as in general in dilute magnetic oxides, DMOs, is associated with surface and bulk intrinsic defects such as Ce vacancies, mixed Ce^{3+}/Ce^{4+} pairs, oxygen interstitials, etc., but mostly with oxygen vacancies [2,7-12] . It was recognized that the number of point and/or extended defects such as grain boundaries, surfaces, etc. and related long range ferromagnetic ordering strongly depends on the methods and conditions of sample preparation. However, the role of a certain type of defect in ferromagnetism as well as the origin of the ferromagnetism itself in un-doped ceria still remains an open question. In the magnetic polaron impurity-band BMP model [12] the shallow donor electrons form bound magnetic polarons that overlap resulting in a spin-split impurity band. Charge transfer from the impurity band to unoccupied 3*d* states at the Fermi level (E_F) of dopant ions is responsible for long-range ferromagnetic order. Oxygen vacancies, specifically singly occupied vacancies (F^+ centers), are the most known defects that can provide *n*-type conduction and thus the shallow donors. Shah et al [11] demonstrated that in TM (e.g. Co) doped CeO_2, ferromagnetism is intimately linked to the oxygen vacancies, capable to mediate the long range coupling among the Ce, as well as among the magnetic impurity spins, even in the absence of itinerant carriers [11]. Their first principle

calculations based on the density functional theory (DFT), prove that the oxygen vacancies can pull the *d* and *f* orbitals of Ce closer to the Fermi level to cause an exchange splitting [11]. In the frame of this theory, the F-center ferromagnetic exchange (FCE) mechanism (a sub category of BMP theory) was applied to explain the FM in magnetic dielectrics/insulators such as CeO_2. However, it is believed that the ferromagnetic ordering associated with F^+ centers could not appear in un-doped ceria with low density of these centers, because they are localized and the F-electron orbital is too large [11,12]. The giant orbital paramagnetism model [13 - 15] where the ferromagnetic response is field induced and originates from coherent mesoscopic conduction (surface) currents refers to the mesoscopic quasi-2D matter (nanoparticle surface, thin films, a thin active surface area of single crystals, etc.) and could explain the occurrence of ferromagnetism in undoped cerium oxide [13]; however, this model deals with anhysteretic magnetization curves. Concerning the charge transfer ferromagnetism model, the defects such as twin boundaries, grain boundaries, surfaces of nanoparticles, etc., are associated with an extended defect band [16,17]. Electron transfer (e.g. from the defects, adsorbate species, (TM) dopants) to the defect states could rise the Fermi level in the local density of states. At a sufficiently high density of states, the Stoner criteria $N(E_F)>1/I$ (where ($N(E_F)$ is the density of states at the Fermi level, and I is the Stoner exchange parameter) can be fulfilled and spontaneous spin-splitting brings about the onset of ferromagnetism. It is considered that such charge transfer cannot occur to any significant extent in undoped materials [17] because the density of states at defects is too small to satisfy the Stoner criterion.

Nevertheless, there are studies which have demonstrated that a high concentration of oxygen vacancies and/or high density of states associated with these defects can induce RTFM in undoped CeO_2 [8, 14, 18]. Singhal et. al. [2] associated ferromagnetism in bulk nondoped CeO_2 with a high density of oxygen vacancies induced by annealing in vacuum - the high density of F^+ centers reduces the F-electron orbital which is crucial to mediate the magnetic coupling. The hybrid functional method shows that kinetically stable oxygen-vacancy clusters, linearly ordered in the ⟨111⟩ direction [19], in the bulk CeO_2 could induce much more dispersive gap states with the weakened electron localization compared with the case of a single vacancy [18]; the electron localization at oxygen vacancy sites (and Ce ions), associated with this ordering, could enhance the ferromagnetism and its stability [18] in un-doped CeO_2.

Concerning the relationship between M_s and defects such as oxygen vacancies

(particularly, revealed by photoluminescence PL measurements) the experimental observations of different laboratories have shown contradictory results [2, 9, 20] – ferromagnetism was consistent or inconsistent with the presence of vacancies. As an example, from magnetic (M_s) and photoluminescence measurements Liu *et al* [20] have concluded that oxygen vacancies do not mediate the ferromagnetism in the CeO_2 nanoparticles.

Finding new sources for defects/oxygen vacancies (or Ce^{3+}) of (nano)ceria is important for potential use not only in spintronics but also in many other applications. The easy of transition between Ce^{4+} and Ce^{3+} oxidation states or high catalytic activity allow the use of (nano)ceria and CeO_2-containing materials (along with more commonly used metal oxides [e.g. 21, 22] and oxide matrices incorporating magnetic nanoparticles [e.g. 23, 24]) in platforms of various relevant compounds and applications: in biology and biomedicine (in multi-bioenzyme mimetic activities, as antioxidant, in therapy) [25], toxicology [25, 26, 27, 28], textile engineering application [e.g. 29], sensing devices [30, 31, 23, 24], energy conversion systems (e.g. solid oxide fuel cells, SOFC) [32], etc. The excellent catalytic activity of nanoceria, Ce(III)- and nanoceria- containing frameworks combined with porous microstructure (or an exceptional large specific surface area) and/or with intrinsic or extrinsic magnetic properties provide opportunities for widespread applications in multifunctional devices especially in the development of new generation sensing tools [33, 30]. Ce(III) paramagnetic complexes (e.g. Ce - MOF, metal oxide frameworks) or nanoceria functionalized with extrinsic species/nanoparticles having a strong and stable magnetic response can be developed (1) as new magnetic resonance imaging, MRI, contrast agents [33] acting as responsive agents (for indication of the pH, redox states, enzymatic activities, etc.), theranostics agents and targeted agents; (2) in magnetic responsive positioning [30] for use in drug delivery for cancer treatment, carcinogenic molecules sequestration, pollution control, in miniaturized probe with sensing capabilities toward e.g. aromatic amines, etc. and (3) in magnetic induction swing adsorption (MISA) [34, 30] for efficient remove of toxic metals from polluted environments, controlled release of adsorbed species from different types of adsorbents, etc.

The aim of this work is to correlate the defects states (associated with the defect-related PL emission in the visible range as well as revealed by differential scanning calorimetry, DSC, Fourier transform infrared spectroscopy, FTIR, and X-ray diffraction, XRD, measurements) with the ferromagnetism found for the first time in un-doped ceria nanopowders produced by

thermal decomposition of Ce-propionate and by annealing in air. Three sources for defects that can provide a large number of oxygen vacancies (density of states) potential to induce or enhance ferromagnetism in un-doped cerium oxide were found and analyzed: (1) defects generated during decomposition of Ce-propionate; (2) oxygen vacancies survived/redistributed (at the surfaces/GBs) upon heating from the starting precursor; (3) oxygen vacancies provided in excess by decomposition of Ce - oxycarbonate residues. In addition, this study provides an explanation for the inconsistency frequently reported in literature between M_s and the intensity of defect-related PL emission or oxygen vacancies – this inconsistency for the ceria nanopowders prepared in air arises from the fact that the surfaces/GBs rather than lattice defects are responsible for high M_s.

2 Experimental

Cerium oxide powders were fabricated by a sol-gel process. Cerium (III) acetate sesquihydrate ($(CH_3CO_2)_3Ce{\cdot}1.5H_2O$, Alfa Aesar, 99.9%) was dissolved in propionic acid (CH_3CH_2COOH, Merck, >99%). The methanol was added in a methanol:propionic acid (with a 1:2 ratio) and this mixture was maintained for several hours under stirring at 60°C until an homogeneous sol was produced; the gel was obtained after further stirring at 80°C. The gel has been dried at 120°C in air and resulted in the precursor powder P (hereinafter referred to as initial precursor powder P or Ce-propionate). Four precursor nanopowders A, B, C and D (hereinafter referred to as starting precursors or precursor (nano)powders A, B, C and D) were prepared by calcination of the Ce-propionate for 120 min, 60 min, 150 min and 180 min at 250°C, 400°C, 460°C and 500°C, respectively in air; the A, B and C precursors were processed under continuous mixing. Annealing of the precursor nanopowders A, B, C and D in air and under the oxygen flux at different temperatures (430°C - 1200°C) for different durations (10 min – 480 min) resulted in four batches of samples: (A, A1, A2), (B, B1, B2), (C, C1,C2) and (D, D1, D2). The annealing conditions are given in Table 1.

Thermal analysis was performed using TG/DSC in a SETARAM Setsys Evolution 18 equipment. The initial precursor powder P / Ce-propionate (33.21 mg weight) was measured in dry air atmosphere between 25°C and 1000°C at a heating rate of 5°C /min with a temperature precision higher than 0.01 °C. The structure of cerium oxide powders was investigated by X-ray diffraction (XRD) performed on a Bruker D8 Advance diffractometer in Bragg–Brentano

geometry using Cu $K_{\alpha 1}$ radiation (wavelength 1.5406 Å). The data were acquired at room temperature, with a step-scan interval of 0.04° - 0.02° and a step time of 1.0 s. The XRD data were processed by Rietveld whole powder pattern fitting using the Bruker-TOPAS software and the fundamental parameter approach (FPA). The Fourier transform infrared (FTIR) spectroscopy measurements were carried out with a Perkin Elmer BX Spectrum spectrometer, in attenuated total reflection mode (Pike-MIRacle diamond head of 1.8 mm in diameter). The analyses were performed within the spectral range 4000-500 cm^{-1} with a 4 cm^{-1} resolution and 64 scans per experiment. The microstructures of the powders were characterized by a FEI Quanta Inspect F scanning electron microscope (SEM). Room temperature Photoluminescence (PL) spectra excited at 295nm have been recorded using a Jobin Yvon Fluorolog Fluoroamax 4P spectrophotometer. For a correct comparison all the samples have been measured in the same conditions. Magnetization measurements of powders were performed using a Quantum Design MPMS-5S SQUID magnetometer at room temperature and an applied magnetic field of up to 24500 Oe.

3 Results and discussions

The DSC, TG and DTG curves recorded on precursor powder P upon heating are shown in Fig.1. The Fourier transform infrared spectroscopy (FTIR) spectra of the initial precursor P, starting precursor A and samples A1, B1, D1 and C1 are shown in Fig. 2. The spectrum of the precursor powder P was identified as propionate $Ce(C_2H_5COO)_3$ [35,36]. Fig. 3 shows the XRD patterns assigned to the fluorite face centered cubic structure (space group *Fm*3*m*5) phase for all samples of sets A, B, C and D. The lattice constants and the crystallites size evaluated from Rietveld fitting of the XRD patterns are listed in the Table 1. As expected, the average grain size increases with the annealing temperature, from few nanometers for the A, B, C and D starting precursors and exceeding 500 nm for samples annealed at 1150°C for longer times (e.g. sample A2). The decrease of lattice constant with the annealing temperature (it ranges between 5.4160 A and 5.4107A, Table 1) is consistent with the increase of grain size in CeO_2 nanopowders [37, 38]. SEM micrographs for nanopowders A, B1 and D1 are shown in Figs. 4a, 4b and 4c, respectively. The dimensions of smallest nanoparticles distinguished by SEM are comparable with the crystallite size determined from XRD patterns (Table 1).

3.1 T*he formation of defective cerium oxide by thermal decomposition of Ce-propionate. The conditions for coexistence of nanocrystaline ceria and* $Ce_2O_2CO_3$.

Thermal analysis (DSC/TG/DTG) correlated with FTIR and XRD analysis allowed the interpretation of the thermal decomposition reactions of Ce propionate. The FTIR spectrum recorded on the initial precursor P (Fig. 2) shows the vibrational bands characteristic for rare-earth propionates at 1548 cm^{-1}, 1290, 1076, 898, and 813 cm^{-1} [35, 39, 40]; the C=O stretching vibration at 1710 cm^{-1} characteristic for the COO^- functional group of the propionic acid initial reactant [39] is not observed. The analysis of TG/DSC, XRD and FTIR measurements indicates that the Ce-propionate powder undergoes decomposition in four stages upon heating.

The first region between 25°C and about 230°C could be ascribed to the dehydration process of the hydrates:

$$Ce(C_2H_5COO)_3 \cdot H_2O \rightarrow Ce(C_2H_5COO)_3 + H_2O \quad (1)$$

The dehydration process is accompanied by a step in mass loss of 1.4% registered at 97°C in TG and is consistent with the presence of an endothermic peak in DSC (Fig. 1). Some H_2O loss was delayed to higher temperatures consistent with the step of mass loss in TG curve at 225°C which might be due to trapping of H_2O inside the powder particles and released when the compound melted. The total mass loss at 237°C (end of the mass loss step), amounts to 5.1%, which is quite close to the 4.8% expected for the release of one H_2O molecule from a formal $Ce(C_2H_5COO)_3 \cdot H_2O$ starting composition [36, 41].

At the second stage the anhydrous $Ce(C_2H_5COO)_3$ is fused [36] in association with the endothermic peak observed in the DSC trace at around 233°C (Fig. 1). The melting process was visually observed during the preparation of the precursor nanopowders A, B and C (from the precursor P) on the hot plate under continuous mixing.

Upon further heating of the fused propionate an intense and complex exothermic effect registered in the DSC curve between 245°C and 340°C (Fig. 1) is accompanied by a significant mass loss in two steps. The rate of mass loss as evaluated from the DTG curve (top-right inset of Fig. 1), is changing from a relatively slow regime from 250°C to 302°C, to a fast rate up to about 340°C. The change in the rate of mass los at 302°C is also visible in TG curve and is highlighted by vertical dashed line in the main panel of Fig. 1. At 302°C, the total weight loss of approximately 24% is close to theoretical expectations for the formation of an intermediate $Ce_2O(C_2H_5COO)_4$ phase as reported as well for the thermal decomposition of lanthanide- and Y-

propionates [35, 36, 41]. This means that anhydride propionate $Ce(C_2H_5COO)_3$ is decomposed to $Ce_2O_2CO_3$ (confirmed by FTIR analysis below) through the $Ce_2O(C_2H_5COO)_4$ intermediate compound by release of 3-pentanone and carbon dioxide, similarly to other reports on related compounds [35,36,40]:

$$2\ Ce(C_2H_5COO)_3 \rightarrow Ce_2O(C_2H_5COO)_4 + C_2H_5COC_2H_5 + CO_2 \quad (2)$$

and

$$Ce_2O(C_2H_5COO)_4 \rightarrow Ce_2O_2CO_3 + 2C_2H_5COC_2H_5 + CO_2 \quad (3)$$

The decomposition of the anhydrous cerium propionate and the formation of $Ce_2O_2CO_3$ are confirmed by the FTIR spectra of the precursor A and sample B1 shown in Fig. 2. A weakening and disappearance of the propionate peaks at 1290 $cm^{-1}$and at 813 cm^{-1} corresponding to wCH_2 and γCH_2, respectively, is observed similarly to a report on the decomposition of Y propionate [35]. The peaks at about 1525 cm^{-1} and 850 cm^{-1}, remaining after the decomposition of cerium propionate, were associated with the antisymmetric and symmetric vibrational mods of CO_3^{2-} [40,42] of the $Ce_2O_2CO_3$ [35 and references therein].

Above 340°C the sample weight continues to decrease up to 1000°C but with a lower rate (top-left inset of Fig. 1). The mass loss in this temperature range is ascribed to the final stage of thermal decomposition of $Ce_2O_2CO_3$ to CeO_2. By analogy to ref. [36] for Ce this decomposition takes place as follows:

$$Ce_2O_2CO_3 + 1/2O_2 \rightarrow 2CeO_2 + CO_2 \quad (4)$$

This decomposition reaction is supported by the decrease of the oxycarbonate peak intensity in the FTIR spectra of D1 (annealed at 615°C for 150 min) and A1 (annealed at 1020°C for 10 min) samples (Fig. 2).

The total mass loss for CeO_2 formation starting from $Ce(C_2H_5COO)_3 \cdot H_2O$ is theoretically 54%, whereas the observed value is 52.1% at 1000°C. This difference is related to the presence of residue of undecomposed $Ce_2O_2CO_3$ (see FTIR curves for D1 and A1 in Fig. 2). This implies that the decomposition of $Ce_2O_2CO_3$ in air would still take place when heating the powder to higher temperatures and/or longer durations. In virtue of the equation (4) the process of the decomposition of Ce-oxicarbonate traces during annealing can influence significantly the concentration of surfaces and GBs oxygen vacancies important for ferromagnetism as will be discussed in next subsection. Carbonaceous residues are usually observed in the products after decomposition of propionates in inert atmosphere [35, 41, 43]. Previous studies of the rare earth-

propionates annealed in inert atmosphere have shown that during decomposition of oxycarbonates the weight decreases continuously up to the temperature at which the decomposition to oxide is complete (up to 1350°C for Y-propionate decomposition in Ar [35]). For the $[La_2(CH_3CH_2COO)_6 \cdot (H_2O)_3] \cdot 3.5H_2O$ the TG curve presents a plateau after the complete $La_2O(CO_3)_2$ oxycarbonate transformation into lanthanum oxide [39]. In the present case the above described process of $Ce_2O_2CO_3$ decomposition is not completed upon continuous heating to 1000°C in air at 5°C/min rate, as also seen from the amount of mass loss in TG shown in the inset of Fig. 1.

As seen from Fig. 3 and Table 1, all the samples (including the A precursor prepared at the lowest temperature 250°C) show ceria phase with fluorite face centered cubic structure. Accordingly, a band in the spectral range of 500 – 600 cm^{-1} assigned to Ce - O vibrational mode of cerium oxide [e.g. 44] is observed for all samples in FTIR (Fig. 2). For the nanopowders treated at lower temperatures, up to 1020°C°, especially for precursor A and sample B1, the Ce – O band is wider with lower intensity and its average position is shifted to higher wavenumbers (~570 cm^{-1}) as compared to the more oxidized sample C1 (annealed at 1150°C for 120 min) where it was observed at 550 cm^{-1}. The relationship between the wavenumber, $\bar{\nu}$, and the average length of Ce - O bond, r, can be written as [45]:

$$\bar{\nu} = \frac{1}{2\pi c}\left(\frac{f}{\mu}\right)^{1/2} \quad (5)$$

$$f = \frac{17}{r^3} \quad (6)$$

where c is the speed of light, f is force constant of Ce – O bond and μ is the reduced mass of Ce – O molecule. In virtue of equations (5) and (6) the above mentioned blue shift can be associated with the presence of defects of oxygen vacancies type in the ceria annealed up to 1020°C (see A, B1, D1 and A1 in Fig. 2). The creation of oxygen vacancies will result in the decrease of force constant and the increase of average length of Ce – O bond. This is in agreement with the obviously higher lattice parameter of samples A and B1 compared to that of more oxidized sample C1 as determined from XRD patterns (Fig. 3, Table 1). As the A precursor (prepared at the lowest temperature, 250°C °C) shows the cerium oxide phase in both XRD and FTIR measurements, this indicates that ceria with a high number defects (hereinafter referred to as defective ceria) was formed during the decomposition stage of Ce-propionate at 245– 340°C

(Fig. 1) after its melting [43]. Taking into account that the defective ceria formed during the thermal decomposition of Ce-oxycarbonate is oxygen deficient, the total mass loss in TG for cerium oxide formation should be even larger than 54%. This gives additional confirmation that the lower value of 52.1% observed at 1000°C is caused by the presence of residual $Ce_2O_2CO_3$ and that the process of the oxycarbonate decomposition could still take place in the ceria powder upon annealing at higher temperatures and/or longer durations. Higher heating rates, as in the case of samples described in the next subsection (in Table 1) which were heated at a rate of 10°C/min, could delay the decomposition of oxycarbonate traces to even higher temperatures. By heating the defective ceria in air the local oxycarbonate decomposition is expected to occur simultaneously with the global oxidation process of Ce^{3+} to Ce^{4+}. This is confirmed by the fact that the samples still containing traces of $Ce_2O_2CO_3$, e.g. D1 annealed at 615°C and A1 annealed at 1020°C (Fig. 2), have their lattice parameter relaxed compared to that of stoichiometric ceria (Table 1). In other words, the process of local oxygen depletion, e.g. at the GBs and surfaces, may take place simultaneously with the global oxidation process, as will be discussed in more details in the next subsection.

Unlike the initial precursor P (Ce-propionate) the FTIR spectra for the A, B1 and D1 samples exhibit a broad band centered at 3335 cm^{-1} corresponding to the vibrations of weakly bound (adsorbed) water interacting with its environment via hydrogen bonding and to vibrations of hydrogen-bonded OH groups. The appearance of this band is most probably related to the cerium oxide formation when its nanosized grains (Fig. 4, Table 1) having a high effective surface area were exposed to ambient atmosphere.

3.2 *Room temperature photoluminescence and ferromagnetism*

In Figs. 5a and 5b are depicted the M vs. H curves measured at room temperature for products of batches A and B, and C and D, respectively. The upper insets display the curves after subtracting the paramagnetic signal whereas the lower insets show the enlarged region close to the origin. The data extracted from the Figs. 5a, b are listed in Table 1. In Fig. 5a the M vs H curve for Ce - propionate (sample P) is also given. Ce-propionate shows a strong paramagnetic response. The un-doped ceria exhibits room temperature ferromagnetism with H_c between 8 Oe and 121 Oe and M_s of up to 6.7×10^{-3} emu/g. All four A, B, C and D precursor nanopowders prepared directly from the Ce-propionate show ferromagnetism with $M_s = 0.21*10^{-3}$, $2.3*10^{-3}$,

$0.29*10^{-3}$ and $4.6*10^{-3}$ emu/g and H_c = 82, 83, 42 and 27 Oe, respectively.

The photoluminescence spectra recorded on the samples from the A and B batches are shown in Figs. 6a and 6b, respectively. All the spectra of samples of batches A, B, C and D show two emission bands: a relatively sharp UV emission centered at about 378 nm (3.25 eV, insets of Figs. 6a and 6b) accompanied by another broad band located in the visible region between 400 nm and 550 nm. The intensity and the integrated area of defect-related PL peaks in the visible light emission for all samples are listed in the Table 1. The UV emission is ascribed to the 2p-4f energy gap (the transition from the 4f band to the valence band) of stoichiometric CeO_2 [46]. As the energy levels of defect states in the cerium oxide are located within the band gap, the broad visible photoluminescence (corresponding to a broad distribution of electronic energy levels between 2.4 and 3.16 eV, insets of Figs. 6a and 6b) is attributable to the defects in ceria. The defects in this work were primarily associated with oxygen vacancies (or Ce^{3+} oxidation states since they are charge-balanced by oxygen vacancies [37, 38]) because upon annealing in air (or in oxygen flow) with increasing temperature/time the defective ceria (described in the previous subsection) behaves commonly to a reduced cerium oxide annealed under oxidative conditions. Indeed, as can be seen from Figs. 5 and Table 1 in the samples annealed in air at temperatures above 1000°C and/or for long durations the intensity/area of the defect related PL peak diminishes. At the same time, the ferromagnetic signal decreases or disappears (A2, C1, C2 and D2 in Table 1) which is direct evidence that the observed ferromagnetism is related to defects (oxygen vacancies) in the cerium oxide. Further evidence of this is given by the PL measurements on the B2 sample annealed in oxygen atmosphere at 1050°C for 180 min that shows a severe decrease of both the defect - related PL peak (Fig. 6a) and of the ferromagnetic signal (Table 1). The weakening of both ferromagnetism and defect - related PL emission is caused by the oxygen vacancies removal from the *whole volume* of the sample when annealing in oxidative conditions at high temperatures and long times. The reduction of oxygen vacancies (the oxidation process) in the defective ceria is supported by the results of XRD (Fig. 3) and FTIR (Fig. 2) measurements already discussed in the previous subsection. By annealing the starting precursor C in air at high temperature, 1150°C, the Ce-O absorption band in FTIR become sharper, it narrows towards lower wavenumbers, from ~570 cm^{-1} (precursor A) to 550 cm^{-1} (sample C1). The global process of oxidation of Ce^{3+} to Ce^{4+} is also confirmed by the overall decrease of the lattice constant with increasing temperature (Fig. 3, Table 1). All these

experimental facts strongly support that the ferromagnetism was induced by defective ceria formed during the decomposition reactions of Ce-propionate.

As will be demonstrated hereinafter, the factors such as the oxidative decomposition of carbonaceous residues and the development of GB network can retain/redistribute or enhance the (local) defect concentration and ferromagnetism upon heating. Indeed, in the samples exhibiting sizable ferromagnetism, > 10^{-4} emu/g, (Fig. 5, Table 1) along with relatively intense defect-related PL emission (Fig. 6), the cerium oxide coexists with $Ce_2O_2CO_3$ traces (Fig. 2). First of all, the presence of carbonaceous residues denotes that the propionate decomposition process or the annealing process (in air) occurred somehow similarly to the same kind of experiments performed in inert atmosphere. In other words, these processes took place in conditions that stimulate the production of vacancies. An analogous coexistence of the oxycarbonate and oxides was reported for the thermal decomposition of Y-propionate to Y_2O_3 [35] in inert atmosphere (the formation of Y_2O_3 was noticed at higher temperatures, than for ceria in the present study, above 600°C as a result of decomposition of oxycarbonates). Secondary, the use in this study a relatively large initial masses (200 – 300 mg) for thermal annealing stimulated the oxygen depletion inside the sample (more acute for powders that were not mixed during annealing (e.g. precursor D) and/or at the bottom of the products) particularly due to the oxidative decomposition of propionate [43] and other carbon containing species. In addition the gas transport is more difficult through higher powder quantities [43].

As already discussed, the overall trend upon annealing in air at higher temperatures and/or longer durations is the decrease of the intensity of defect-related PL emission and M_s. However, we have observed that the defect related PL emission and the ferromagnetism remain unchanged or even increase after certain conditions of annealing (Figs. 5, 6 and Table 1). The intensity (area) of defect-related PL emission increased by a factor of about 1.75 (1.72) and M_s increased from 0.21 emu/g to 1.4 emu/g when the A precursor was annealed at 1020°C for short time, 10 min (sample A1) (Figs. 5a, 6a and Table 1). The same behavior was observed for the B precursor annealed at 430°C for 90 min (sample B1): the intensity (area) of defect - related PL emission has increased with a factor of about 1.69 (1.47) and M_s increased from 2.3 to 6.7 emu/g (Figs. 5a, 6a and Table 1). The FTIR spectra show the presence of $Ce_2O_2CO_3$ (the spectrum for B is similar to those for A and B1 shown in the Fig. 2) for all these four samples, A, A1, B and B1. The main differences which were found between A (prepared at 250°C) and A1 (annealed

at 1020°C) as well as between B (prepared at 400°C) and B1 (annealed at 430°C) are the crystallite size and lattice constant (Fig. 3, Table 1). The increase of crystallites in A1 (from 7.4 nm to 75 nm) and in B1 (from 6.9 nm to 7.5 nm) is associated with GB development in these two nanopowders annealed at higher temperatures compared with the started precursors A and B. A confirmation is given by the SEM micrographs of the precursor A (prepared at 250°C) (Fig. 4a) and sample B1 (annealed at 430°C) (Fig. 4b) with comparable crystallite size: the relatively isolated nanoparticles in the initial aggregates (precursor A) tend to fuse together when annealing at higher temperatures (sample B1) to create GBs. This evolution of the microstructure is very evident in the SEM imeges taken from different scaned areas of sample D1 anealed at 615°C for 150 min – it can be seen how the isolated nanoparticles first evolve into the nanocrystals separated by GBs within the grains (main panel and inset of Fig. 4c) and then avolve into biger cristals (main panel of Fig. 4c). Once the GBs start to develop during annealing of A1 and B1 samples the incorporation of the oxygen from the air inside the sample is more difficult compared with the A and B starting precursors. Hence, the sintering of nanoparticles and the development of GBs could induce a *local* oxygen depletion or the conservation/redistribution of a large number of oxygen vacancies from the defective ceria of the starting precursors, contributing in this way to the increase of M_s. The higher ability of GBs to adsorb/trap the impurities (here vacancies) than the free surfaces was reported by others [47]. The ferromagnetism generated by defects such as oxygen vacancies at free surfaces of oxides is frequently reported [8, 14, 18]. However, the total solubility of impurity elements (e.g. transition metal atoms) at GBs of fine grained oxide samples (e.g. ZnO) is much higher than at the surfaces: GBs can adsorb up to 10 monolayers of ion of transition metals whereas free surfaces adsorb only 2-4 monolayers [47-49]. Concerning the conservation and redistribution of oxygen vacancies from the starting precursors, sample A1 obtained by annealing of precursor A at 1020°C for 10 min presents an evidence of this. The defect - related photoluminescence or vacancies concentration of sample A1 enhanced substantially whereas the lattice constant, on the contrary, relaxed to the value of 5.4107(1) Å (as compared to 5.4128(5) Å of the starting precursor A) characteristic for stoichiometric ceria (Fig. 5a, Table 1). This contradiction implies that GBs (surfaces) rather than lattice vacancies are responsible for enhanced M_s of A1 sample (this aspect will be discussed in more details hereinafter in this work). An explanation is that during heating at 1020°C the oxygen vacancies migrated from the grain interior towards GBs

where they were trapped.

The *local* oxygen depletion inside the sample, described in the previous paragraph, will be more powerful if the development of GB network or the sintering of nanoparticles begins before the decomposition of $Ce_2O_2CO_3$ (or other species containing C) to cerium oxide is completed. This is well visible for samples A1 and D1. The grain size has increased (i.e. the GBs network has developed) from 10.4 nm to 13 nm when the D precursor was annealed at 615°C (sample D1) and from 7.4 nm to 75 nm when the A precursor was annealed at 1020 °C (sample A1). At the same time, the intensities of the absorption bands in FTIR associated to Ce-oxicarbonate decreased considerably for D1 and A1 (Fig. 2). Nevertheless, residual $Ce_2O_2CO_3$ traces being still present in coarser grained A1 and D1 implies that decomposition of oxycarbonate to cerium oxide occurred at the better developed GB network compared with the starting precursor nanopowders A and B (Fig. 4). As already emphasized, the decomposition reaction or annealing with the carbonaceous residues left behind is a signature of the almost inert local environment ([43] and references therein). An important recent founding is that in inert atmosphere some Ce alkanoates decompose via $Ce_2O_2CO_3$ first to Ce_2O_3 which is then oxidized to CeO_2 [50]:

$$Ce_2O_2CO_3 \rightarrow Ce_2O_3 + CO_2 \quad (7)$$

$$Ce_2O_3 + ½\ O_2 \rightarrow 2CeO_2 \quad (8)$$

In the present case of annealing in air the stability of Ce_2O_3 is improbable. Instead, the XRD and FTIR analyses indicate that $Ce_2O_2CO_3$ decomposes to cerium oxide between two stoichiometric forms Ce_2O_3 and CeO_2: partially to near stoichiometric CeO_2 and partially to CeO_{2-x} (where x is the vacancy concentration) with higher nonstoichiometry. An important feature of ceria is that the fluorite crystal structure can survive at very high vacancy concentrations, $1.7 \leq 2\text{-}x \leq 2$ (see e.g. [51] and references therein]. A careful inspection of the Ce – O band (inset of Fig. 2) reveal that the above described blue shift with decrease of annealing temperature is in fact the development of a new component corresponding to 595 cm^{-1} vibrational frequency besides that at 550 cm^{-1}. The Ce – O band found at the highest wavelength, 595 cm^{-1}, could be associated with the surface phonon modes generated when the wavelength of the incident radiation is higher than the particle size [52, 53]. The interaction of electromagnetic radiation with the particles depends as well on the state of aggregation of the crystals [53]. Thus, the 595 cm^{-1} band relates

to the absorption by the surface states at lower sizes. In virtue of equations (5) and (6) and the discussions therein this surfaces states in highly nonstoichiometric cerium oxide, CeO_{2-x}, could be identified with the oxygen vacancies. 595 cm^{-1} band is well visible for the powders with the smallest grain size (A and B1 in Fig. 2) and correspondingly with the higher lattice parameter (Table 1). With increasing annealing temperature the 595 cm^{-1} band intensity decrease (D1 and A1 in Fig. 2) until it disappears for the well oxidized sample (C1 in Fig. 2). In this way, when annealing in air Ce^{3+} can originate directly from the decomposition of $Ce_2O_2CO_3$ residues whereas the local Ce^{3+} to Ce^{4+} oxidation is slow at the GBs and at the nanoparticle surfaces (in the specific conditions e. g. inside the powders that were not mixed during annealing). Thus, *extra* oxygen vacancies were produced at the GBs by the decomposition of $Ce_2O_2CO_3$ traces. This could be a reason for the increased area of defect-related PL luminescence (Fig. 6) and improvement of ferromagnetism (Fig. 5) in the samples A1 and B1, compared with A and B starting powder precursors. In addition, as shown hereinbefore, because of the short annealing at quite high temperature, 1020°C, without continuous mixing, followed by a high cooling rate from this temperature, a large amount of oxygen vacancies was retained from the defective ceria of starting precursor A at the GBs in sample A1. Another example of residues influence on the sample properties is an observed delay effect of the grain growth: the D2 sample, annealed at 1020°C for 150 min in air, shows 93 nm nanocrystals size as compared to B2 sample, annealed in similar conditions at 1050°C for 180 min but in oxygen atmosphere, shows 256 nm nanocrystals size (Table 1). In air the carbonaceous residues decomposition rate was lower than in oxygen atmosphere and therefore their presence at the GBs inhibited the grain growth. The understanding of the processes occurring at the surfaces/GBs upon annealing of ceria prepared by chemical route is very important not only for ferromagnetism and its use in spintronics [5, 6]) but also for many other applications, e.g for the performance of superconductors for which CeO_2 serves as one of the most suitable template for the superconducting layers ([43, 54-56] and references therein).

For the samples belonging to the same batch the intensity/area of defect-related PL emission correlates with the ferromagnetic properties (Table 1). This is obvious from Fig. 7, for the samples derived from the same starting precursor (A, B, C or D) showing that M_s is proportional to the area of defect-related PL peak. However, this behavior cannot be generalized to the samples belonging to different batches as this is also visible in the same Fig. 7. This

inconsistency is often reported in literature. This is very evident for the A, B, C and D starting precursors themselves, which all show nanocrystals size < 10.4 nm and higher lattice constants compared with the stoichiometric ceria of samples treated at high temperatures (e.g. A2, B2, C1, C2 and D2 in Table 1). The FTIR spectra of all four samples are similar (and similar to that for A shown in Fig. 2) showing Ce-O bands at ~570 cm^{-1} assigned to the defective ceria as noticed in previous subsection beside the characteristic $Ce_2O_2CO_3$ bands. Nonetheless, ferromagnetic properties (e.g. M_s) and their relationship with the intensity of defect-related PL emission are very different for these four products (Figs. 5, 6 and Table 1). For example, in the C precursor the ferromagnetism (M_s) is much weaker as compared to B and D precursors whereas the difference in the intensity/area of defect-related PL emission is less significant and inconsistent with the M_s values: M_s for the C sample is only $0.29*10^{-3}$ emu/g compared with $2.3*10^{-3}$ emu/g for B and $4.6*10^{-3}$ emu/g for D. The observed discrepancy can be explained in the simplest way as caused by the differences in the *local* density of defects, at the surfaces of nanoparticles or at the GBs in aggregates/grains. In turn, the local density of defects is dependent on the decomposition degree of carbonaceous species, $Ce_2O_2CO_3$, or related production degree of vacancies in excess. As already discussed, the surface concentration of oxygen vacancies (defects) would be higher when the process of annealing in air is interrupted before the process of the decomposition of carbonaceous species has completed (or saturated). In other words, the surface concentration of oxygen vacancies depends on the rate of decomposition of the carbonaceous species at the moment of interruption of annealing process. The decomposition rate should be higher at higher temperature but is also dependent on the annealing time, (local) partial oxygen pressure and other parameters that determine the kinetics of the combustion process [41]. The annealing of the D precursor was performed at the highest temperature (at 500 °C for 240 min) among all four precursors presuming an advanced development of the GB network. Most important is that the precursor D was processed without mixing during annealing which together with the development of GBs implied a restricted access of oxygen inside the sample/aggregates. In turn, a relatively inert environment inside the sample delayed the decomposition of carbon-containing species. Hence, the process of excess production of oxygen vacancies (at the nanoparticles surface or at the newly developed GBs) still continues when the annealing is interrupted. The same is valid for precursor nanopowder B annealed by continuous mixing but at lower temperature and shorter duration (400°C for 60 min). An excess of oxygen

vacancies at the nanoparticles surface and at the GBs, is consistent with high values of the M_s observed for both B and D precursors (Table 1). Mingjie Li et al [9] reported a similar relationship between RTFM and the reduction degree of the surface of CeO_2 nanoparticles when hydrogen was used as reducing agent (see also [57]). As for the precursor nanopowder A, annealed at significantly lower temperature, 250°C, by continuous mixing for 120 min, the decomposition rate of carbonaceous species was slower. The excess defects at the nanoparticles surface were produced with lower rate and, in addition, were removed by the prolonged annealing in air, which is consistent with lower values of M_s observed for A precursor compared with the B and D precursors. On the other hand, the intensity of defect-related photoluminescence (associated with both surface/GBs and bulk defects) of the A precursor do not differ significantly from that of the B precursor (Fig. 6, Table 1). Finally, the annealing of the nanopowder precursor C was performed by continuous mixing (and thereby by increased exposure of the particles surface to the ambient oxygen) at relatively high temperature and for long duration (460°C for 150 min). In these conditions, the carbon-containing compounds have burned with high rate, however during the longer annealing time the excess of defect states at the nanoparticles surface has been removed as for the A sample. As a consequence, a low M_s value (0.29 emu/g) was observed in the C sample, even if it shows a global concentration of defects (intensity/area of the defect-related PL peak) higher than that of precursor B with superior M_s value of 2.3 emu/g (Table 1).

Therefore, the precursors B and D / A and C show high/low M_s values primarily because the annealing was interrupted in the process of production/removing of oxygen vacancies resulting from the consumption of carbonaceous residues, i.e. $Ce_2O_2CO_3$, at the nanoparticle surface or at the GBs in aggregates/grains. These differences in the reduction degree of the surface of nanoparticles for different starting precursors, the fact that the M_s of nanosized cerium oxide prepared in air is more susceptible to modifications of the concentration of surface and GBs defects rather than to bulk/lattice density of defects and that both surfaces/GBs and bulk vacancies make a contribution to PL emission in the visible range could be the reasons of the inconsistency between the saturation magnetization and the defect - related photoluminescence signal when all the samples belonging to different batches are considered. In other words, the inconsistency between M_s and the intensity of defect-related PL emission or oxygen vacancies arises from the fact that the surfaces/GBs rather than lattice defects are responsible for high M_s.

(In this context, note the universal behavior of the photoluminescence and of the intrinsic RT ferromagnetic order induced by the surfaces or near-surfaces disordering/defects when comparing the results of nanosized ceria system studied in this work as well as reported by others [e.g. 58] with the one of the most studied oxides, ZnO, in very different forms and preparation conditions, e.g metal ion implanted ZnO crystals [59, 60], un-doped ZnO nanopowders prepared by hydrothermal rout [61], un-doped ZnO thin films [62], gas ion implanted ZnO single crystals [63], etc.). Sample A1, discussed hereinbefore, obtained by annealing of precursor A at 1020°C for 10 min, presents strong evidence that the surfaces/GBs rather than lattice vacancies are responsible for enhanced M_s: the defect - related photoluminescence or vacancies concentration along with M_s enhanced substantially whereas the lattice constant, on the contrary, relaxed to the value characteristic for stoichiometric ceria (Figs. 5a and 6a, Table 1). The defects such as oxygen vacancies on the surfaces and at the GBs are more exposed and their concentration is more sensitive to the modifications of the local environment during annealing in air than the bulk defects. Finely, it is evident that the nature of the relationship between the M_s and defect-related PL (Fig. 7) is primarily driven by the quality of starting precursors (A, B, C and D) prepared directly through the thermal decomposition of Ce - propionate.

4 Conclusions

In summary, RTFM and a broad defect-related photoluminescence PL emission were observed for the first time in cerium oxide nanopowders successfully prepared by means of Ce-propionate decomposition and annealing in air. An improvement of the intensity of defect-related PL emission and of ferromagnetism was obtained for products in which the nanocrystaline cerium oxide coexists with Ce-oxycarbonate traces. For the samples prepared from the same starting precursor the M_s is proportional to the intensity of defect-related PL emission whereas inconsistency between these two parameters is observed for the samples prepared from different precursors. Three sources of defects, and thus of the ferromagnetism in un-doped cerium oxide were identified. (1) The high concentration of defect states (e.g. oxygen vacancies), produced during thermal decomposition of Ce-propionate initial precursor. (2) Oxygen vacancies from the defective ceria of the precursors can survive/redistribute under annealing conditions that promote an inert *local* environment: annealing without continuous mixing, when the sintering of nanoparticles begins (e.g. in the presence of GBs), short annealing time, annealing in large

masses, high cooling rate, etc.. (3) Decomposition of $Ce_2O_2CO_3$ residues to cerium oxide provides an excess of oxygen vacancies at the GBs or at the nanoparticles surfaces resulting in the enhancement of ferromagnetism. The differences in the reduction degree of the surface of nanoparticles for different samples, the fact that M_s of nanosized ceria is more susceptible to the modification of the concentration of surface and/or GBs defects rather than to bulk density of defects and that PL emission in the visible range includes the influence of both surfaces/GBs and lattice oxygen vacancies can explain the inconsistency between the saturation magnetization and the intensity of defect-related photoluminescence signal.

The three sources for defects/oxygen vacancies in nanograined CeO_2 identified in this work deserve further investigations for potential use of related RTFM in spintronics. However, these findings along with other results of the present study are essential for use of nanoceria in other important applications as follows:

- Our SQUID measurements reveal that prepared in this study Ce - propionate have a strong paramagnetic signal. Paramagnetic complexes are able to modify their behavior upon interaction with (bio/macro)molecules in the specific microenvironment, e.g. via interaction with a biomarker. Thus, Ce(III) propionate paramagnetic complexes or Ce(III) complexes functionalized by propionate ligands (Ce-MOFs) could be developed as magnetic resonance imaging (MRI) contrast agents. Ce(III) complexes are the agents that may produce MRI contrast through the mechanisms such as PARACEST and PARASHIFT that have attracted recent interest. Ce-MOFs being functionalized by extrinsic magnetic species to prepare porous Ce-magnetic framework composite, Ce-MFCs, and being exposed to a DC or AC external magnetic field may be used in (miniaturized) sensing devices.

- The nano-sized grains in A, B, B1, C and D powders forming the frameworks with high porosity and thus with large surface area, the high activity (enhanced lattice parameter determined by XRD), the high degree of crystallinity as well as the potential for postsynthetic modification makes nanoceria frameworks (eventually functionalized by extrinsic magnetic species) promising candidates for applications (described in Introduction) that involve the high catalytic activity, e.g. for biosensing applications.

- The results of our study on the decomposition of Ce-propionate indicates the possibility to obtain the ceria nanocrystals coated with Ce-carbonate as new approach for ceria - carbonate nanocomposite electrolyte for low temperature solid oxide fuel cells (LT-SOFC).

Acknowledgement

The authors gratefully acknowledge the financial support from the Core Program PN18 of Ministry of Education of Romania (MEdC). The authors would like to express their gratitude to I. Pasuk and G. Stan for their help in the experimental and technical work.

References

[1] V. Fernandes, P. Schio, R. J.O. Mossanek, A. J.A. de Oliveira, W. A. Ortiz, D. Demaille, F. Vidal, Y. Zheng, P. Fichtner, L. Amaral, M. Abbate, J. Varalda, W. H. Schreiner, D. H. Mosca (2011) Anisotropy of magnetization and nanocrystalline texture in electrodeposited CeO films. Electrochem Solid-State Lett. 14: 9

[2] R. K. Singhal, P. Kumari, A. Samariya, S. Kumar, S. C. Sharma, Y. T. Xing, E. B. Saitovitch (2010) Role of Electronic Structure and Oxygen Defects in Driving Ferromagnetism in Nondoped Bulk CeO_2. Appl Phys Lett 97: 172503

[3] A. Tiwari, V. M. Bhosle, S. Ramachandran, N. Sudhakar, J. Narayan, S. Budak, A. Gupta (2006) Ferromagnetism in Co doped CeO_2: Observation of a giant magnetic moment with a high Curie temperature. Appl Phys Lett 88:142511

[4] A. Sundaresan, R. Bhargavi, N. Rangarajan, U. Siddesh, C. N. R. Rao (2006) Ferromagnetism as a universal feature of nanoparticles of the otherwise nonmagnetic oxides. Phys Rev B 74:161306

[5] S. A. Wolf, D. D. Awschalom, R. A. Buhrman, J. M. Daughton, S. von Molnar, M. L. Roukes, A. Y. Chtchelkanova, D. M. Treger (2001) Spintronics: A Spin-Based Electronics Vision for the Future. Science 294:1488

[6] K. M. Krishnan, A. B. Pakhomov, Y. Bao, P. Blomqvist, Y. Chun, M. Gonzales, K. Griffin, X. Ji , B. K. Roberts (2006) Nanomagnetism and spin electronics: materials, microstructure and novel properties. J Mater Sci 41:793–815

[7] M. Venkatesan, C. B. Fitzgerald, J. M. D. Coey (2004)Thin films: Unexpected magnetism in a dielectric oxide. Nature 430: 630

[8] V. Fernandes, R. J. O Mossanek, P. Schio, J. J. Klein, A. J. A de Oliveira, W. A. Ortiz, N. Mattoso, J. Varalda, W. H. Schreiner, M. Abbate, D. H. Mosca (2009) Dilute-defect Magnetism: Origin of Magnetism in Nanocrystalline CeO_2. Phys Rev B 80:035202

[9] M. Li, S. Ge, Wen Qiao, Li Zhang, Yalu Zuo, Shiming Yan (2009) Relationship between the surface chemical states and magnetic properties of CeO_2 nanoparticles. Appl Phys Lett 94: 152511

[10] M. Y. Ge, H. Wang, E. Z. Liu, J. Z. Jiang, Y. K. Li, Z. A. Xu, and H. Y. Li (2008) On the origin of ferromagnetism in CeO_2 nanocubes. Appl Phys Lett 93:062505

[11] L. R. Shah, B. Ali, H. Zhu, W. G. Wang, Y. Q. Song, H. W. Zhang, S. I. Shah, and J. Q. Xiao (2009) Detailed study on the role of oxygen vacancies in structural, magnetic and transport behavior of magnetic insulator: Co– CeO_2. J Phys: Condens Matter 21:486004

[12] J. M. D. Coey, M. Venkatesan, and C. B. Fitzgerald (2005) Donor impurity band exchange in dilute ferromagnetic oxides. Nature Mater 4:173

[13] J.M.D. Coey, K. Ackland, M. Venkatesan, S. Sen (2016) Collective magnetic response of CeO_2 nanoparticles. Nature Physics 12:694

[14] K. Ackland, L. M. A. Monzon, M. Venkatesan, J. M. D. Coey (2011) Magnetism of Nanostructured CeO_2. IEEE Trans Magn 47:3509

[15] J. M. D. Coey, M Venkatesan, P Stamenov (2016) Surface magnetism of strontium titanate. J Phys: Condens Matter 28:485001

[16] J. M. D. Coey, P. Stamenov, R. D. Gunning, M. Venkatesan, K. Paul (2010) Ferromagnetism in defect-ridden oxides and related materials. New J Phys 12:053025

[17] J. M. D. Coey, K. Wongsaprom, J. Alaria, M. Venkatesan (2008) Charge-transfer ferromagnetism in oxide nanoparticles. J Phys D: Appl Phys 41:134012

[18] X. Han, N. Amrane, Z. Zhang, M. Benkraouda (2016) Oxygen Vacancy Ordering and Electron Localization in CeO_2: Hybrid Functional Study. J Phys Chem C 120:13325

[19] S. Hull, S. T. Norberg, I. Ahmeda, S. G. Eriksson, D. Marrocchelli, P. A. Madden (2009) Oxygen vacancy ordering within anion-deficient Ceria. Journal of Solid State Chemistry 182: 2815

[20] Y. Liu, Z. Lockman, A. Aziz, J. MacManus-Driscoll (2008) Size dependent ferromagnetism in cerium oxide (CeO_2) nanostructures independent of oxygen vacancies. J Phys: Condens.Matter 20:165201

[21] Angel Ezhilarasi, J. Judith Vijaya, K. Kaviyarasu, M. Maaza, A. Ayeshamariam, L. John Kennedy (2016) Green synthesis of NiO nanoparticles using *Moringa oleifera* extract and their

biomedical applications: Cytotoxicity effect of nanoparticles against HT-29 cancer cells. Journal of Photochemistry and Photobiology B: Biology doi:10.1016/j.jphotobiol.2016.10.003

[22] K. Kaviyarasu, C. Maria Magdalane, E. Manikandan, M. Jayachandran, R. Ladchumananandasivam, S. Neelamani, M. Maaza (2015) Well-Aligned Graphene Oxide Nanosheets Decorated with Zinc Oxide Nanocrystals for High Performance Photocatalytic Application International Journal of Nanoscience 14 (03):1550007

[23] J. Leveneur, G. I. N. Waterhouse, J. Kennedy, J. B. Metson, D. R. G. Mitchell (2011) Nucleation and Growth of Fe Nanoparticles in SiO2: A TEM, XPS, and Fe L-Edge XANES Investigation. J. Phys. Chem. C 115 (43): 20978-20985

[24]) J. Leveneur, J. Kennedy, G. V. M. Williams, J. Metson, A. Markwitz. (2011) Large room temperature magnetoresistance in ion beam synthesized surface Fe nanoclusters on SiO2. Appl. Phys. Lett. 98:053111

[25] Can Hu and Xiaogang Qu (2014) Cerium oxide nanoparticle: a remarkably versatile rare earth nanomaterial for biological applications. NPG Asia Materials 6, e90

[26] C. Maria Magdalane, K. Kaviyarasu, J. Judith Vijaya, C. Jayakumar, M. Maaza, B. Jeyaraj (2017) Photocatalytic degradation effect of malachite green and catalytic hydrogenation by UV–illuminated CeO_2/CdO multilayered nanoplatelet arrays: Investigation of antifungal and antimicrobial activities. Journal of Photochemistry and Photobiology B: Biology 169:110-123

[27] C. Maria Magdalane, K. Kaviyarasu, J. Judith Vijaya, B. Siddhardha, B. Jeyaraj (2017) Facile synthesis of heterostructured cerium oxide/yttrium oxide nanocomposite in UV light induced photocatalytic degradation and catalytic reduction: Synergistic effect of antimicrobial studies. Journal of Photochemistry and Photobiology B: Biology 173:23-34

[28] C. Maria Magdalane, K. Kaviyarasu , J. Judith Vijaya, Busi Siddhardha, B. Jeyaraj (2016) Photocatalytic activity of binary metal oxide nanocomposites of CeO_2/CdO nanospheres: Investigation of optical and antimicrobial activity. Journal of Photochemistry and Photobiology B: Biology 163:77-86

[29] C. Maria Magdalane, K. Kaviyarasu, J. Judith Vijaya, Busi Siddhardha, B. Jeyaraj, J. Kennedy, M. Maaza (2017) Evaluation on the heterostructured CeO2/Y2O3 binary metal oxide nanocomposites for UV/vis light induced photocatalytic degradation of Rhodamine - B dye for textile engineering application. Journal of Alloys and Compounds 727:1324-1337

[30] P. Falcaro, R. Ricco, C. M. Doherty, K. Liang, A. J. Hill, M. J. Styles (2014) MOF positioning technology and device Fabrication. Chem. Soc. Rev. 43:5513

[31] K. Kaviyarasu, Xolile Fuku, Genene T. Mola, E. Manikandan, J. Kennedy, M. Maaza (2016) Photoluminescence of well-aligned ZnO doped CeO2 nanoplatelets by a solvothermal route. Materials Letters 183:351-354

[32] Liangdong Fan, Chuanxin He, Bin Zhu (2017) Role of carbonate phase in ceria–carbonate composite for low temperature solid oxide fuel cells: A review. Int. J. Energy Res. 41/4:465–481

[33] S. E. Miller, M. H. Teplensky, P. Z. Moghadam, D. Fairen-Jimenez (2016) Metal-organic frameworks as biosensors for luminescence-based detection and imaging. Interface Focus 6: 20160027

[34] H. Li, M. M. Sadiq, K. Suzuk , R. Ricco, C. Doblin, A. J. Hil , S. Li , P. Falcar , M. R. Hill (2015) Magnetic Metal–Organic Frameworks for Efficient Carbon Dioxide Capture and Remote Trigger Release. Advanced Materials DOI: 10.1002/adma.201505320

[35] J. -C. Grivel (2013) Thermal decomposition of yttrium (III) propionate and butyrate. J Anal Appl Pyrolysis 101:185

[36] M. Ogawa, K. Manabe (1993) Formation of dilanthanide monoxide tetrapropionate by thermal decomposition of propionate monohydrate of rare-earth elements (La, Ce, Pr, Nd). Nippon Kagaku Kaishi 5:617

[37] Feng Zhang, Siu-Wai Chan, Jonathan E. Spanier, Ebru Apak, Qiang Jin, Richard D. Robinson, Irving P. Herman (2002) Cerium oxide nanoparticles: Size-selective formation and structure analysis. Appl Phys Lett 80:127

[38] S. Tsunekawa, K. Ishikawa, Z. Q. Li, Y. Kawazoe, and Y. Kasuya (2000) Origin of Anomalous Lattice Expansion in Oxide Nanoparticles. Phys Rev Lett 85:3440

[39] L. Ciontea, M. Nasui, T. Jr. Petrisor, R. B. Mos, M. S. Gabor, R. A. Varga, T. Petrisor (2010) Synthesis, crystal structure and thermal decomposition of $[La_2(CH_3CH_2COO)_6\_(H_2O)_3]\_3.5H_2O$ precursor for high-k La_2O_3 thin films deposition. Mater Res Bull 45:1203

[40] M. Nasui M, C. Bogatan (Pop), L. Ciontea, T. Petrisor (2012) Synthesis, crystal structure modeling and thermal decomposition of yttrium propionate $Y_2(CH_3CH_2COO)_6\_H_2O]\_3.5H_2O$. J Anal Appl Pyrolysis 97:88

[41] J.-C. Grivel (2014) Thermal decomposition of $RE(C_2H_5CO_2)_3\_H_2O$ (RE: Dy, Tb,

Gd, Eu and Sm). J Therm Anal Calorim115:12534

[42] A.N. Christensen, Hydrothermal Preparation of Neodymium Oxide Carbonate (1970) The Location of the Carbonate Ion in the Structure of $Nd_2O_2CO_3$. Acta Chemica Scandinavica 24: 2440

[43] P. Roura, J. Farjas, J. Camps, S. Ricart, J. Arbiol, T. Puig, X. Obradors (2011) Decomposition processes and structural transformations of cerium propionate into nanocrystalline ceria at different oxygen partial pressures. J Nanopart Res 13:4085

[44] K.Kaviyarasu, E.Manikandan, Z.Y.Nuru, M.Maaza (2015) Investigation on the structural properties of CeO_2nanofibers via CTAB surfactant. Materials Letters 160: 61-63

[45] R. E. Mallawany (1989) Theoretical and experimental IR spectra of binary rare earth tellurite glasses – 1. Infrared Phys. 29: 781 - 785

[46] S. Y. Chen, C. H. Tsai, M. Z. Huang, D. C. Yan, T.W. Huang, A. Gloter, C. L. Chen, H. J. Lin, C.T. Chen, C. L. Dong (2012) Concentration Dependence of Oxygen Vacancy on the Magnetism of CeO2 Nanoparticles. J Phys Chem C 116:8707

[47] B. B. Straumal, S. G. Protasova, A. A. Mazilkin, T. Tietze, E. Goering, G. Schütz, P. B. Straumal, B. Baretzky (2013) Ferromagnetic behaviour of Fe-doped ZnO nanograined films. Beilstein J Nanotechnol 4:361

[48] B. B. Straumal, A. A. Mazilkin, S. G. Protasova, A. A. Myatiev, P. B. Straumal, B. Baretzky (2008) Increase of Co solubility with decreasing grain size in ZnO. Acta Mater 56: 6246

[49] B. Straumal, B. Baretzky, A. Mazilkin, S. Protasova, A. Myatiev, P. Straumal (2009) Increase of Mn solubility with decreasing grain size in ZnO. J Eur Ceram Soc 29:1963

[50] J.-C. Grivel, M.J. Suarez Guevara, Y. Zhao, X. Tang, P.G.A.P Pallewatta, J. Bednarčík, A. Watenphul (2017) Thermal behavior and decomposition of cerium(III) butanoate, pentanoate and hexanoate salts upon heating in argon. J Anal Appl Pyrolysis (accepted)

[51] M. Mogensen, N. M. Sammes, G. A. Tompsett (2000) Physical, chemical and electrochemical properties of pure and doped ceria. Solid State Ionics 129: 63–94

[52] B. Cheng, Y. Xiao, G. Wu, L. Zhang (2004) The vibrational properties of one-dimensional ZnO:Ce nanostructures. Appl. Phys. Lett. 84: 416

[53] K. Yamamoto, C. D. Tran, H. Shimizu, K. Abe (1977) Optical Surface Phonon Modes in ZnO Small Crystals J. Phys. Soc. Jpn. 42: 587-590

[54] L. Ciontea, T. Ristoiu, R.B. Mos, M. Nasui, T. Petrisor Jr, M.S. Gabor, A. Mancini, A. Rufoloni, G. Celentano, T. Petrisor (2012) Epitaxial growth of CeO_2 thin film on cube textured NiW substrate using a propionate-based metalorganic deposition (MOD) method. Materials Chemistry and Physics 133:772– 778

[55] V. Mihalache, N. Stefan, I. Enculescu, N. Mihailescu, M. Socol, M. Miroi (2014) The Influence of the Microstructure and Morphology of CeO_2 Buffer Layer on the Properties of YBCO Films PLD Grown on Ni Tape. J Supercond Nov Magn 27: 2475

[56] V. Mihalache, I. Pasuk (2011) Grain growth, microstructure and surface modification of textured CeO_2 thin films on Ni substrate. Acta Mater 59:4875

[57] R.K. Singhal, Sudhish Kumar, Arvind Samariya, M. Dhawan, S.C. Sharma, Y.T. Xing (2012) Investigating the mechanism of ferromagnetic exchange interaction in non-doped CeO_2 with regard to defects and electronic structure. Materials Chemistry and Physics 132:534

[58] K. Kaviyarasu, P.P. Murmu, J. Kennedy, F.T. Thema , Douglas Letsholathebe, L. Kotsedi, M. Maaza (2017) Structural, optical and magnetic investigation of Gd implanted CeO2 Nanocrystals. Nuclear Instruments and Methods in Physics Research B 409 147-152

[59] J. Kennedy, G. V. M. Williams, P. P. Murmu, B. J. Ruck (2013) Intrinsic magnetic order and inhomogeneous transport in Gd-implanted zinc oxide Physical Review B 88/21:214423

[60] P. P. Murmu, J. Kennedy, G. V. M. Williams, B. J. Ruck, S. Granville, S. V. Chong (2012) Observation of magnetism, low resistivity, and magnetoresistance in the near-surface region of Gd implanted ZnO. Appl. Phys. Lett. 101: 082408

[61] V. Mihalache, M. Cernea, I. Pasuk (2017) Relationship between ferromagnetism and, structure and morphology in un-doped ZnO and Fe-doped ZnO powders prepared by hydrothermal route. Current Applied Physics 17/8:1127-1135

[62] P. Zhan, W. Wang, C. Liu, Y. Hu, Z. Li, Z. Zhang, P. Zhang, B. Wang, X. Cao (2012) Oxygen vacancy - induced ferromagnetism in un-doped ZnO thin films. J. Appl. Phys. 111: 033501–033505

[63] J. Kennedy, P.P. Murmu, E. Manikandan, S.Y. Lee (2014) Investigation of structural and photoluminescence properties of gas and metal ions doped zinc oxide single crystals. Journal of Alloys and Compounds 616:614-617

Figure Captions

Fig. 1 DSC and TG curves for precursor P (Ce-propionate). Top-left inset: detail of the TG curve between 300° C and 1000°C. Top-right inset: DTG curve.

Fig. 2 FTIR spectra of samples A, B1, D1, A1 and C1. Inset: detail of the FTIR spectra near Ce – O band. The curves are shifted upward for clarity.

Fig. 3 X-ray diffraction patterns for cerium oxide products of batch A, B, C and D. The most intense (111) reflection was normalised to unity for all of the samples. The curves are shifted upward for clarity.

Fig. 4 SEM micrographs for (a) starting precursor A, (b) sample B1 and (c) sample D1.

Fig. 5 *M* vs. *H* curves measured at room temperature for cerium oxide products of batches (a) A and B, and (b) C and D. Upper inset: *M* vs. *H* curves after subtracting the paramagnetic signal. Lower inset: *M* vs. *H* curves at the origin. For the sake of clarity the curve for the C1 sample is not shown. In Fig. 5a the *M* vs *H* curve for Ce - propionate (sample P) is also given.

Fig. 6 Room temperature luminescence spectra excited at 295nm for cerium oxide powders of (a) batch A and (b) batch B.

Fig. 7 M_s variation with the increase of area of defect – related PL peak for cerium oxide products of batches A, B, C and D.

Table Captions

Table 1 Preparation conditions, XRD results, magnetic parameters and photoluminescence data for cerium oxide products of batches A, B, C and D. The digit in parentheses is associated with the error on the last digit of the experimental value.

Fig. 1

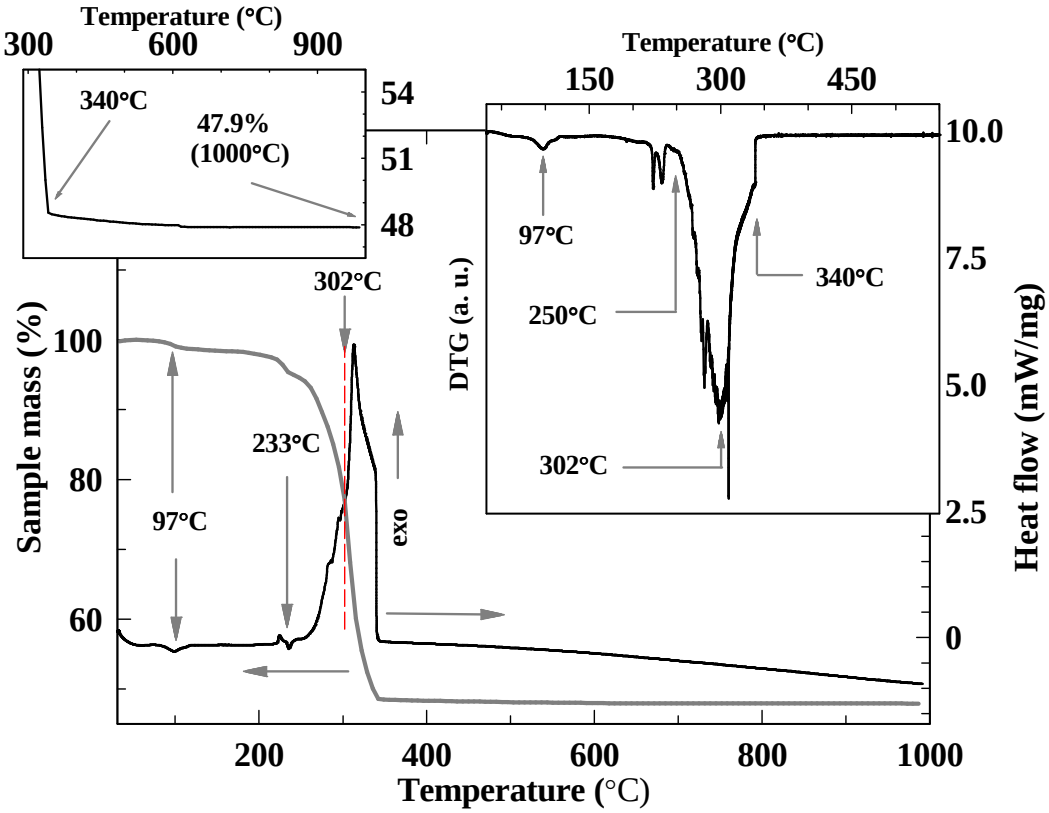

Fig 2

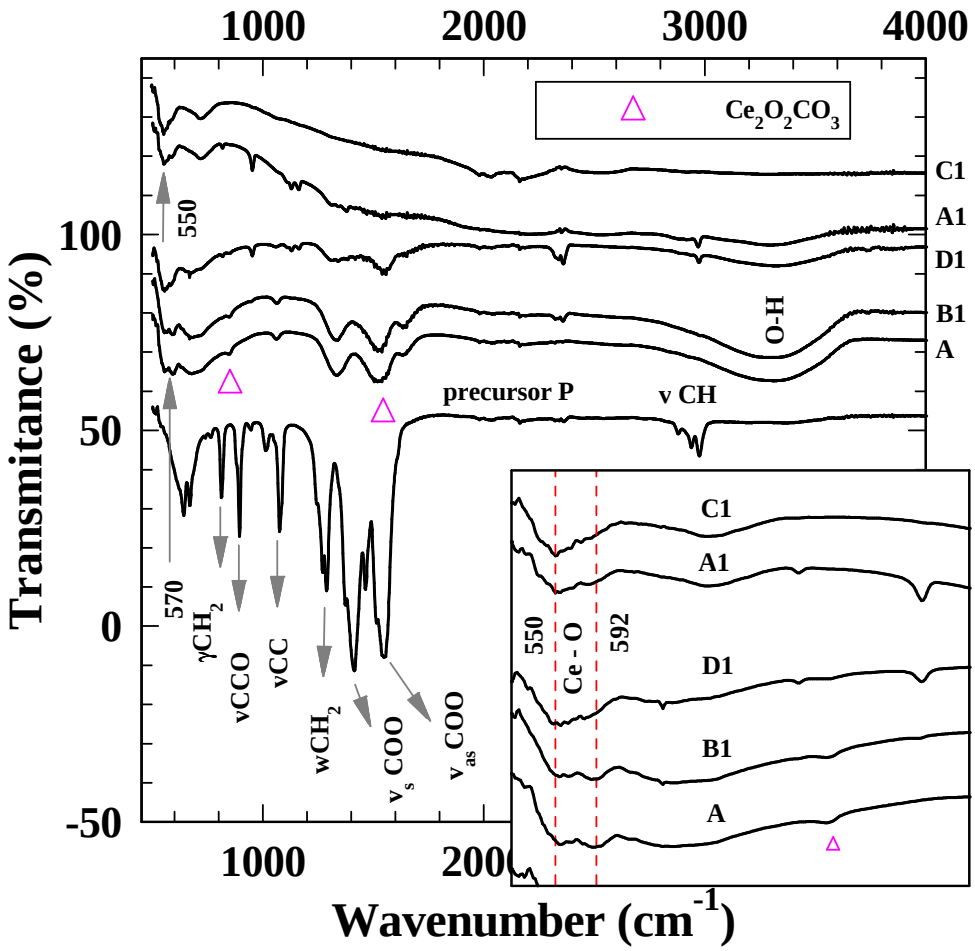
1000
2000
3000
4000
Ce2O2CO3
C1
A1
D1
B1
A
550
O-H
precursor P
v CH
100
50
0
-50
Transmitance (%)
570
γCH2
vCCO
vCC
wCH2
vs COO
vas COO
550
Ce - O
592
1000
200
Wavenumber (cm-1)

Fig 3

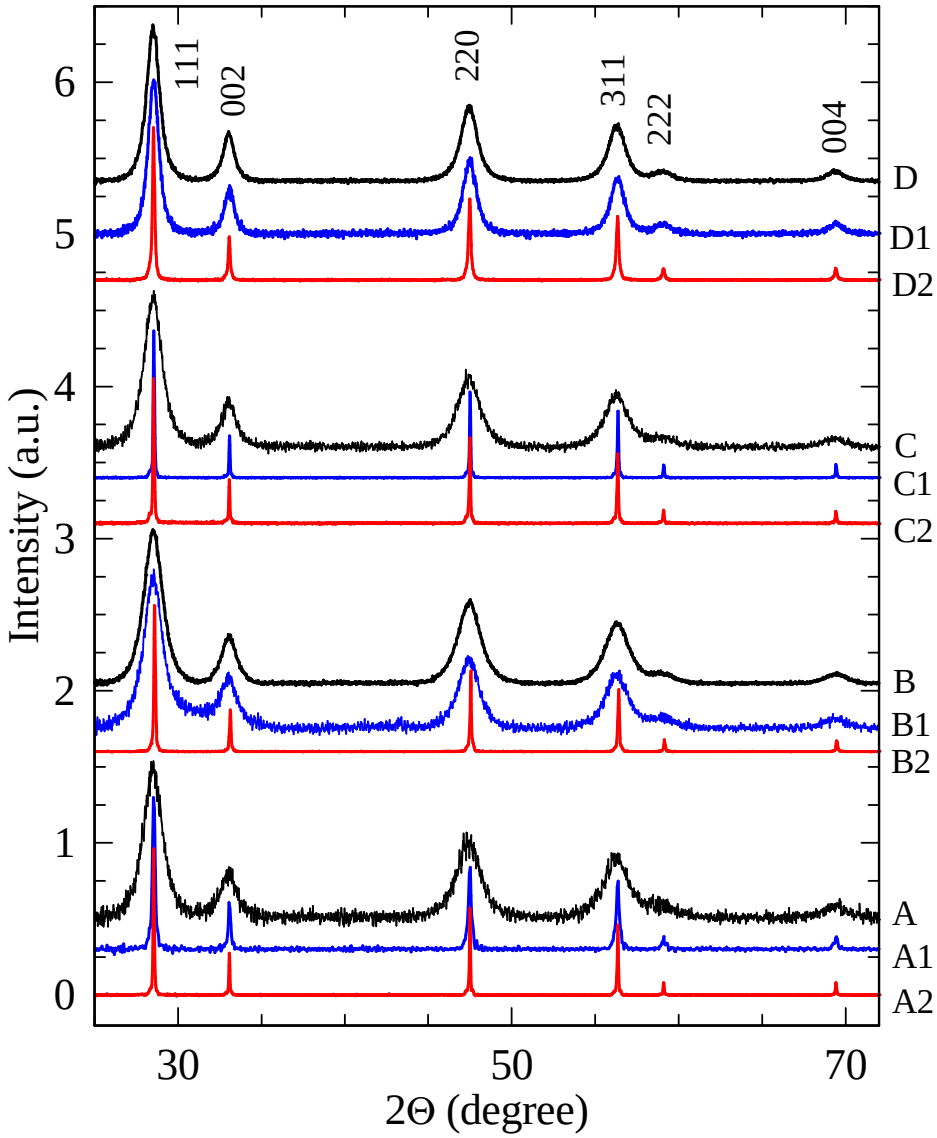

Fig. 4

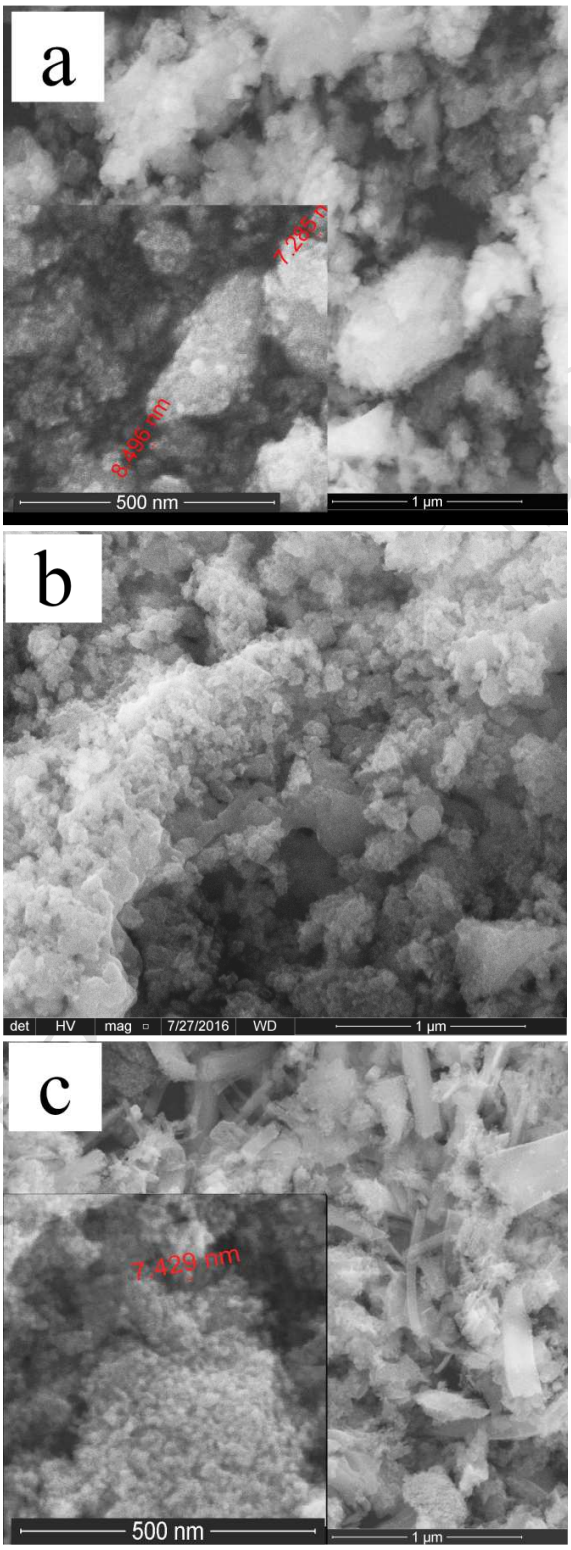

Fig. 5a

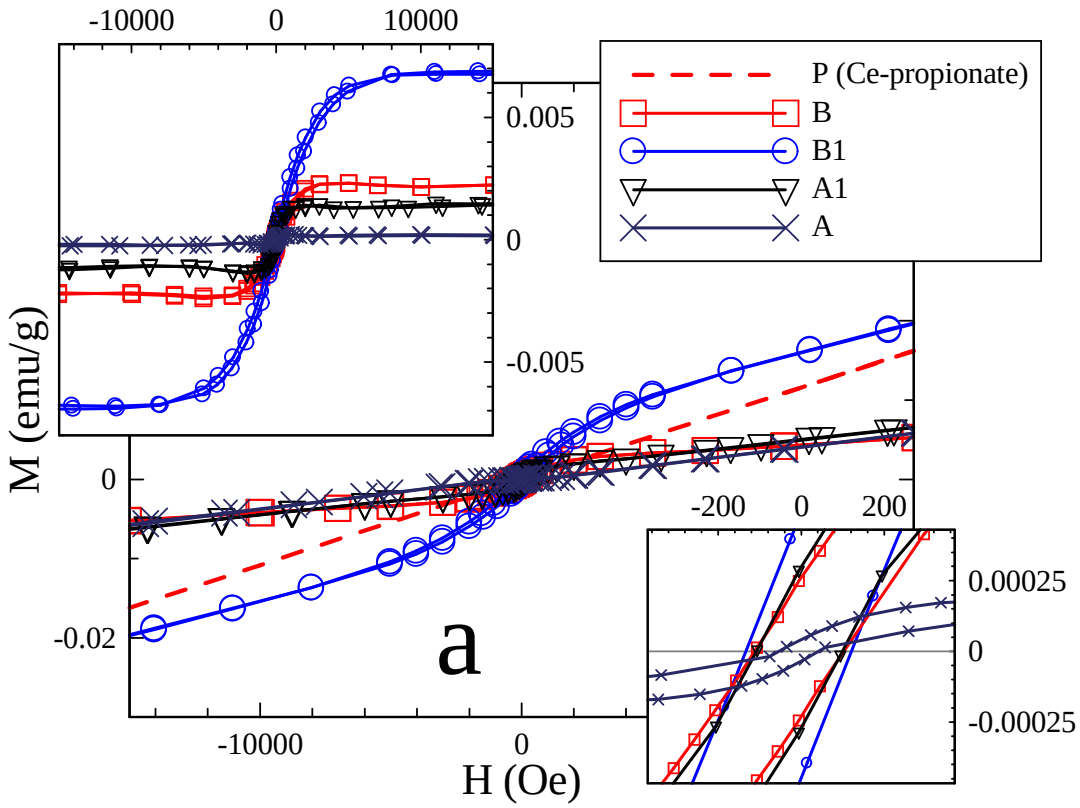
-10000
0
10000
0.005
0
-0.005
P (Ce-propionate)
B
B1
A1
A
M (emu/g)
0
-0.02
-200
0
200
0.00025
0
-0.00025
a
-10000
0
H (Oe)

Fig 5b

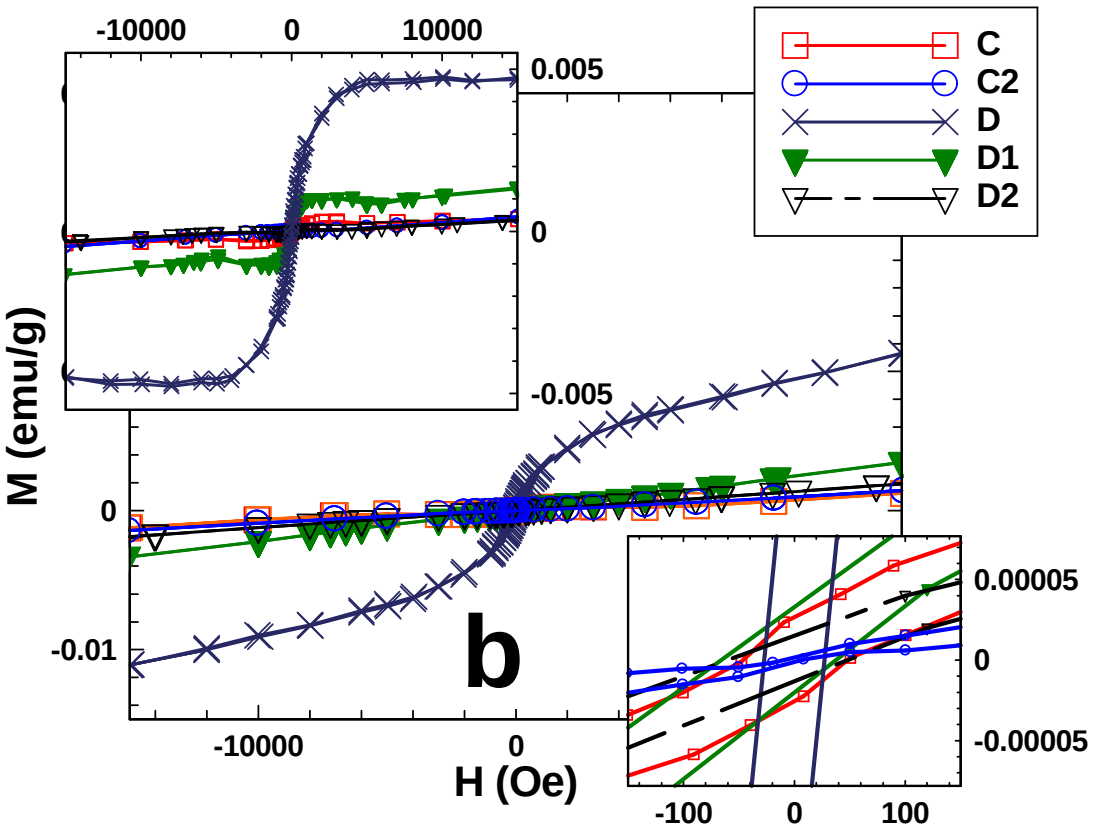
C
C2
D
D1
D2
M (emu/g)
H (Oe)
b
-10000
0
10000
0.005
0
-0.005
-0.01
0.00005
-0.00005
-100
100

Fig 6a

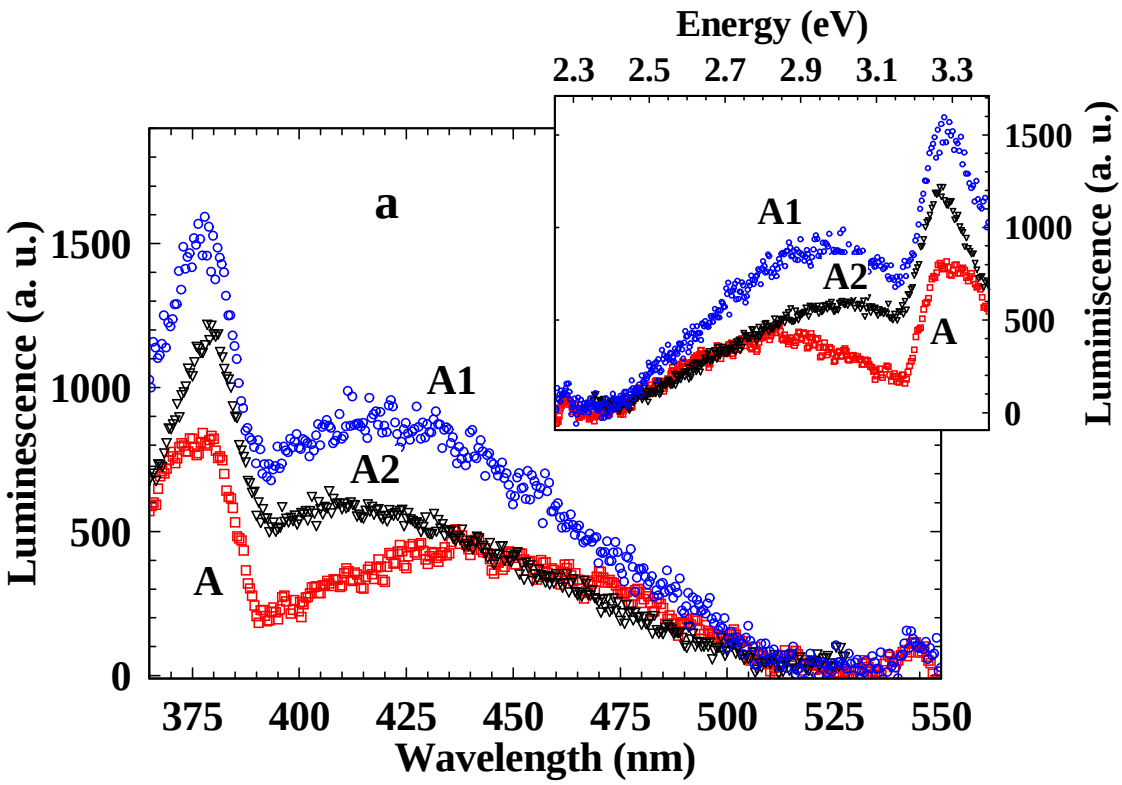

Fig. 6b

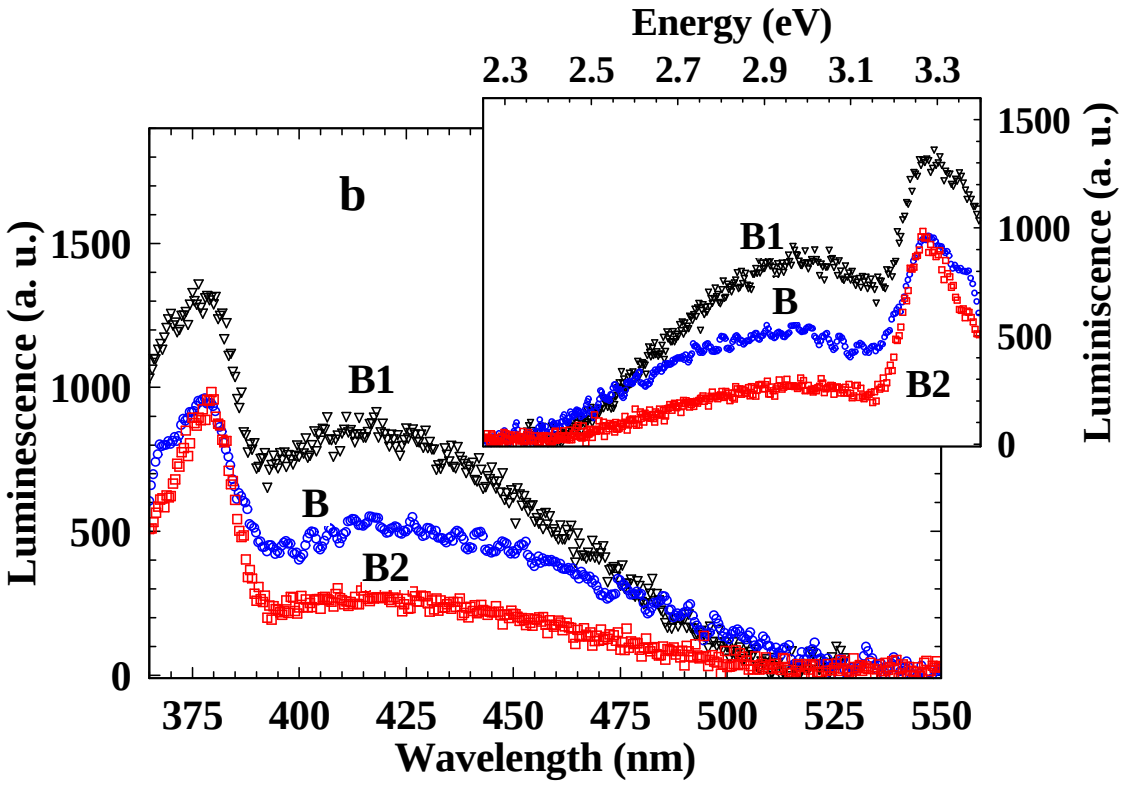
b
B1
B
B2
Luminescence (a. u.)
Wavelength (nm)
Energy (eV)
Luminiscence (a. u.)

Fig. 7

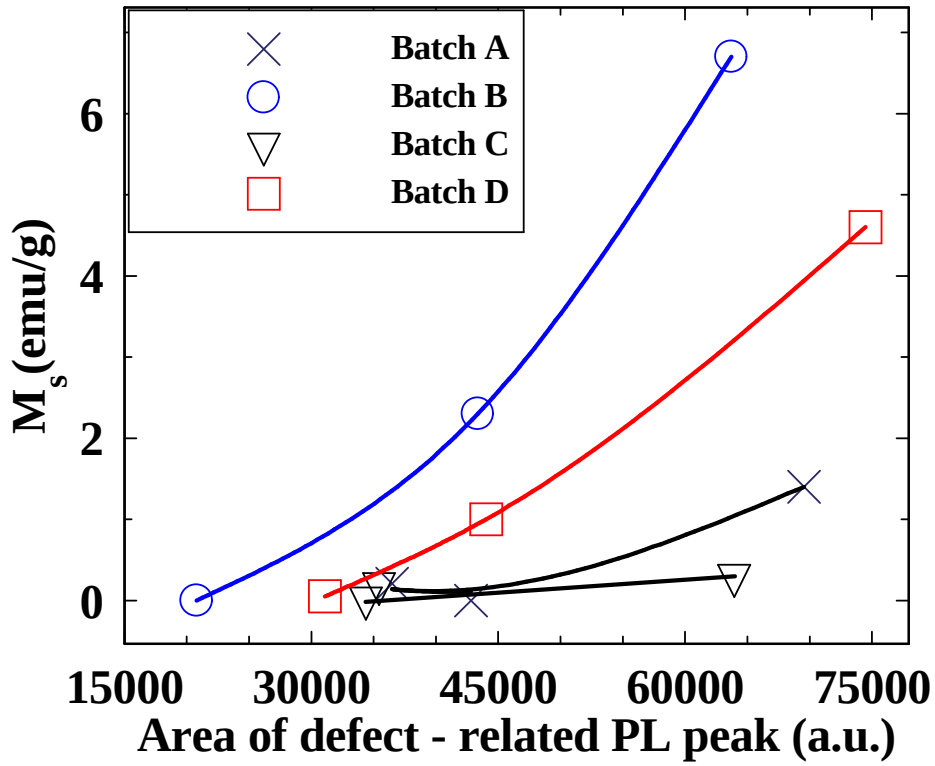
Batch A
Batch B
Batch C
Batch D
6
4
2
0
M_s (emu/g)
15000
30000
45000
60000
75000
Area of defect - related PL peak (a.u.)

Table 1 Preparation conditions, XRD results, magnetic parameters and photoluminescence data for cerium oxide products of batches A, B, C and D. The digit in parentheses is associated with the error of the last digit of the experimental value.

Sample	Preparation conditions		Magnetic parameters		Defect - related PL emission		Crystallite size (nm)	Lattice constant (A)
	Annealing temperature (°C)	Annealing time (min)	M_s (10^{-3} emu/g)	H_c (Oe)	Intensity (a. u.)	Area (a. u.)		
Batch A (starting precursor A and the samples A1 and A2 derived from the precursor A)								
A[a]	250	120	0.21	82	453	36470	7.4(7)	5.4128(5)
A1[b]	1020	10	1.4	104	877	69531	75 (2)	5.4107(1)
A2	1150	120	-	-	580	42808	572(22)	5.4109(1)
Batch B (starting precursor B and the samples B1 and B2 derived from the precursor B)								
B[a]	400	60	2.3	106	505	43375	6.9(5)	5.4147(4)
B1	430	90	6.7	121	854	63708	7.5(6)	5.4160(5)
B2[c]	1050	180	-	-	240	20793	256(3)	5.4108(1)
Batch C (starting precursor C and the samples C1 and C2 derived from the precursor C)								
C [a]	460	150	0.29	42	598	63944	8.3(6)	5.4143(4)
C1	1150	120	0.19	23	485	35426	466(2)	5.4110(9)
C2 [b]	1200	20	0.01	8	426	34375	314(9)	5.4109(2)
Batch D (starting precursor D and the samples D1 and D2 derived from the precursor D)								
D	500	240	4.6	27	763	74472	10.4(7)	5.4144(3)
D1	615	150	0.94	51	548	44023	13(1)	5.4110(2)
D2	1020	150	0.05	54	375	31097	93(8)	5.4110(3)

[a] Continuous mixing; [b] Rapid cooling; [c]Annealed in oxygen atmosphere